INTERNATIONAL JOURNAL OF
NUMERICAL ANALYSIS AND MODELING
Volume 22, Number 5, Pages 614–636

doi: 10.4208/ijnam2025-1027

A FINITE ELEMENT METHOD FOR ANISOTROPIC CRYSTAL GROWTH ON SURFACES

HARALD GARCKE AND ROBERT NÜRNBERG

Abstract. Phase transition problems on curved surfaces can lead to a panopticon of fascinating patterns. In this paper we consider finite element approximations of phase field models with a spatially inhomogeneous and anisotropic surface energy density. The problems are either posed in $\mathbb{R}^3$ or on a two-dimensional hypersurface in $\mathbb{R}^3$. In the latter case, a fundamental choice regarding the anisotropic energy density has to be made. One possibility is to use a density defined in the ambient space $\mathbb{R}^3$. However, we propose and advocate for an alternative, where a density is defined on a fixed chosen tangent space, and is then moved along geodesics to the other tangent spaces. Our numerical method can be employed in all of the above situations, where for the problems on hypersurfaces the algorithm uses parametric finite elements. We prove an unconditional stability result for our schemes and present several numerical experiments, including for the modelling of ice crystal growth on a sphere.

Key words. Crystal growth, hypersurface, phase field, anisotropy, finite elements, stability.

1. Introduction

Crystal growth on curved surfaces can lead to a multitude of interesting patterns. This phenomenon is one example of a phase change problem on a surface. Other applications involve phase separation on surfaces, the formation of two phases in vesicles or in lipid raft formation, see [1, 14, 35, 37, 42, 45, 49, 50, 52, 54, 63]. In this paper we numerically approximate interface evolutions on manifolds governed by an inhomogeneous, anisotropic interfacial energy by using a phase field approach. A particular application we have in mind is dendritic ice crystal growth on surfaces like soap bubbles, see, e.g., the fascinating pictures in [1], partly reproduced in Figure 1. Other possible applications are dendritic growths on aircraft bodies or metal shaped bodies, see [60], and phase separation on surfaces, see [54, 53, 30, 52, 42]. In the latter case one solves a Cahn–Hilliard equation on a surface with either an isotropic or an anisotropic surface energy.

Although phase field models in the Euclidean space have received a lot of attention, see [44, 40, 26, 61, 58, 59, 29, 3], not much is known for (anisotropic) phase field approaches for interface evolution problems on surfaces. Similarly, while for anisotropic phase field models in the Euclidean space a lot is known for the analysis and numerical analysis, see [33, 61, 43, 10, 11, 38, 39] and the references therein, not much is known for anisotropic models on surfaces.

There have been some numerical computations for phase field models describing crystal growth on surfaces, see [50, 63, 45]. However, no numerical analysis has been performed so far. In what follows, we will first introduce the governing equations leading to an anisotropic phase field model on a surface. This system reduces to an anisotropic Cahn–Hilliard equation in situations in which some terms involving time derivatives are neglected. On a surface the interfacial energy is defined on the tangent spaces of the surface. Here, a reasonable choice on how to choose the

Received by the editors on March 21, 2024 and, accepted on October 6, 2024.
2000 *Mathematics Subject Classification.* 35K55, 58J35, 65M12, 65M60, 74E15, 74N20, 80A22, 82C26.

anisotropy when the tangent space changes has to be taken, in order to model physically realistic situations. We basically consider two cases. In the first case we fix an anisotropy in $\mathbb{R}^3$ and then restrict the anisotropy to the respective tangent spaces. The advantage is that the anisotropic density need not depend on space, and existing physical models and numerical methods can be easily extended from flat domains to surfaces. However, it will turn out that this choice has certain undesirable properties. A second choice is obtained by moving an anisotropy given on one fixed tangent space along geodesics to the other tangent spaces. This allows, for example, to choose a six-fold anisotropy on all tangent spaces, see Section 3.2.

For the numerical analysis, we generalize anisotropies introduced by Barrett, Garcke and Nürnberg in [4, 10, 12] to the surface case. This enables us to show stability bounds as well as to prove existence and uniqueness results for fully discrete approximations. These results are shown both for the case of a smooth potential, as well as for the case of an obstacle potential. We remark that the anisotropies can also depend on space, i.e., they can be inhomogeneous. We will then demonstrate the effect of an inhomogeneous energy with the help of numerical simulations. In addition, we will show the effect of different choices of the anisotropy. In particular, in the case where a 3d-anisotropy is restricted to the tangent spaces, the form of the anisotropy can change heavily from tangent space to tangent space. We observe a change from a six-fold anisotropy to a four-fold anisotropy. Moreover, a convergence experiment is presented using an explicit solution constructed by Rätz in [52]. Finally, computations for spinodal decomposition and crystal growth are also presented, where the latter leads to snow crystal growth on manifolds.

Let us now discuss literature related to this work. Basic information on parametric methods for curvature flow and its anisotropic variants can be found in [26, 51, 31, 6, 15, 16, 27, 28, 3]. Related are also the works [47, 48] for curvature flows on graphs. In the computer graphics literature also anisotropies on manifolds have been used and we refer to [56, 57, 64] for details. Phase separation on manifolds using the Cahn–Hilliard model on surfaces has been studied numerically in [54, 30, 52, 42, 22, 49]. Analytic results for inhomogeneous anisotropies can be found in [19, 2, 27].

The outline of this paper is as follows. In Section 2 we present the governing phase field equations on a surface in its strong and weak formulation. In Section 3 we present the different choices of the anisotropy and state and prove certain qualitative properties. Section 4 is devoted to a fully discrete finite element approximation of the anisotropic phase field equations on surfaces. We also state existence, uniqueness and stability results. Their proofs are mostly straightforward extensions of the results in [12] to surfaces and to spatially dependent anisotropies. Finally in Section 5 we present several numerical computations which demonstrate convergence as well as several qualitative properties of solutions.

2. The mathematical model and its weak formulation

2.1. The underlying anisotropic interfacial energy. Let $\mathcal{M} \subset \mathbb{R}^3$ be a given stationary smooth manifold, with or without boundary. We let n denote a continuous unit normal field on $\mathcal{M}$, and m the outer conormal on $\partial\mathcal{M}$. Let $(\Gamma(t))_{t\in[0,T]}$ be a family of evolving curves on $\mathcal{M}$. Then we consider a general anisotropic energy of the form

$$\mathcal{E}(\Gamma) = \int_\Gamma \gamma(z, \nu_{\mathcal{M}}(z))\, \mathrm{d}\mathcal{H}^1(z) = \int_\Gamma \gamma(\cdot, \nu_{\mathcal{M}})\, \mathrm{d}\mathcal{H}^1,$$

FIGURE 1. Freezing of a soap bubble deposited on an ice disk. Taken from [1, Fig. 2]. This figure is used under a Creative Commons Attribution 4.0 license (CC BY 4.0). No changes have been made to the original photograph.

where $\gamma : \mathcal{M} \times \mathbb{R}^3 \to \mathbb{R}_{\geq 0}$ is a given anisotropic energy density that is spatially inhomogeneous and absolutely one-homogeneous in the second argument. In addition, $\nu_{\mathcal{M}}$ denotes a geodesic normal field to Γ on $\mathcal{M}$, i.e., it lies in the normal space of Γ and in the tangent space of $\mathcal{M}$. We always denote by $\mathrm{d}\mathcal{H}^d$, $d \in \mathbb{N}$, integration with respect to the d-dimensional Hausdorff measure. For more information about the geometry of curves and surfaces we refer to [16, 6].

For what follows, we assume that $\Gamma(t)$ separates the manifold into two regions: $\mathcal{M}_\pm(t)$ with $\mathcal{M} = \overline{\mathcal{M}_+(t)} \cup \overline{\mathcal{M}_-(t)}$ and $\Gamma(t) = \overline{\mathcal{M}_+(t)} \cap \overline{\mathcal{M}_-(t)}$. From now on we assume that $\nu_{\mathcal{M}}$ points into $\mathcal{M}_+(t)$. See, e.g., [6].

The sharp interface problem for anisotropic crystal growth on a manifold is the surface Stefan problem with surface tension and kinetic undercooling. To define the flow we introduce κ_γ, the anisotropic geodesic curvature of $\Gamma(t)$, see below for a precise definition, and the velocity $\mathcal{V}$ of $\Gamma(t)$ in the direction of the normal $\nu_{\mathcal{M}}$. We then seek w defined on $\mathcal{M}$, which depending on the setting can be either a temperature field or a concentration field, such that

$$\vartheta w_t - \nabla_s \cdot (\mathcal{K} \nabla_s w) = 0 \qquad \text{in} \quad \mathcal{M}_+(t) \cup \mathcal{M}_-(t), \tag{1a}$$

$$a w = \alpha \kappa_\gamma - \rho \mathcal{V} / \beta(\cdot, \nu_{\mathcal{M}}) \qquad \text{on} \quad \Gamma(t), \tag{1b}$$

$$\lambda \mathcal{V} = -[\mathcal{K} \nabla_s w \cdot \nu_{\mathcal{M}}] \qquad \text{on} \quad \Gamma(t), \tag{1c}$$

where $[.]$ denotes the jump of a quantity across the interface, β is a kinetic mobility and ϑ, $\mathcal{K}$, a, α, ρ, λ are physical parameters, which for simplicity are assumed to be constant. The system then needs to be closed with boundary conditions for w on $\partial\mathcal{M}$, as well as initial conditions for $\Gamma(0)$ and possibly $w(0)$. We note that in the case $\vartheta = 0$ we obtain the surface Mullins–Sekerka problem. In addition, ∇_s denotes the surface gradient on $\mathcal{M}$, and we define similarly the surface divergence and the surface Laplacian, $\Delta_s = \nabla_s \cdot \nabla_s$, see, e.g., [16]. Finally, the anisotropic geodesic curvature is defined as the first variation of the energy $\mathcal{E}$, so that $\kappa_\gamma = -\nabla_s \cdot (P_{\mathcal{M}} \gamma_p(\cdot, \nu_{\mathcal{M}}))$, see, e.g., [6], where $\gamma_p = (\gamma_{p_1}, \gamma_{p_2}, \gamma_{p_3})^T$ denotes the first derivatives of γ with respect to the second argument, and where

$$P_{\mathcal{M}} = \mathrm{Id} - \mathrm{n} \otimes \mathrm{n}$$

is the projection on the tangent space of $\mathcal{M}$. Similarly to [11], we now introduce a corresponding phase field model, where in a first step we replace $\mathcal{E}(\Gamma)$ by an analogue for a diffuse interface.

Following [46, 62, 25, 34, 32], we define

$$A(z,p) = \tfrac{1}{2}\gamma^2(z,p), \qquad z \in \mathcal{M}, p \in \mathbb{R}^3.$$

On introducing a phase field parameter $\varphi : \mathcal{M} \to \mathbb{R}$, where later on $\mathcal{M}_\pm(t) \approx \{z \in \mathcal{M} : \pm\varphi(z,t) > 0\}$, we consider the anisotropic Ginzburg–Landau energy

$$\mathcal{E}_\varepsilon(\varphi) = \int_{\mathcal{M}} \varepsilon A(\cdot, \nabla_s\varphi) + \varepsilon^{-1}\Psi(\varphi)\,\mathrm{d}\mathcal{H}^2, \tag{2}$$

where $\varepsilon > 0$ is an interfacial parameter and $\Psi : \mathbb{R} \to [0,\infty]$ is a suitable potential function. In this work we consider either the smooth double-well potential

$$\Psi(s) = \tfrac{1}{4}(1-s^2)^2, \quad s \in \mathbb{R}, \tag{3}$$

or the double-obstacle potential

$$\Psi(s) = \Psi_0(s) + \mathbb{I}_{[-1,1]}(s), \quad s \in \mathbb{R}, \tag{4}$$

where $\Psi_0(s) = \frac{1}{2}(1-s^2)$ and $\mathbb{I}_{[-1,1]}$ stands for the indicator function of the interval $[-1,1]$, see [21], i.e., $\mathbb{I}_{[-1,1]}$ is zero on $[-1,1]$ and ∞ outside of the interval $[-1,1]$. Note that (2) is the natural generalization of well-known phase field free energies in the flat case to the case of a smooth manifold studied here. We refer to [32, 33, 26, 10, 12] for more details in the flat case.

In the following presentation, for ease of exposition, we assume that Ψ is smooth. Rigorous arguments involving the obstacle potential (4) involve subdifferentials and variational inequalities. We leave these details to the reader, see also [10, 12], and make them more precise when we state our numerical approximations.

2.2. Strong formulation. Given the Ginzburg–Landau energy (2), for a given $\varepsilon > 0$ and Ψ, in this paper we want to study the general anisotropic surface phase field equations

$$\vartheta w_t + \tfrac{1}{2}\lambda\varphi_t - \nabla_s \cdot (\mathcal{K}\nabla_s w) = 0, \tag{5a}$$

$$\tfrac{1}{2}c_\Psi a w = \rho\varepsilon\mu(\cdot,\nabla_s\varphi)\varphi_t - \alpha\varepsilon\nabla_s \cdot (P_{\mathcal{M}} A_p(\cdot,\nabla_s\varphi)) + \alpha\varepsilon^{-1}\Psi'(\varphi) \tag{5b}$$

on $\mathcal{M}$, together with suitable boundary and initial conditions for w and φ. Here

$$\begin{aligned}\nabla_s \cdot (P_{\mathcal{M}} A_p(\cdot,\nabla_s\varphi)) &= \nabla_s \cdot A_p(\cdot,\nabla_s\varphi) - \nabla_s \cdot ((A_p(\cdot,\nabla_s\varphi)\cdot \mathrm{n})\mathrm{n}) \\ &= \nabla_s \cdot A_p(\cdot,\nabla_s\varphi) - A_p(\cdot,\nabla_s\varphi)\cdot \mathrm{n}\nabla_s \cdot \mathrm{n} \\ &= \nabla_s \cdot A_p(\cdot,\nabla_s\varphi) + H_{\mathcal{M}} A_p(\cdot,\nabla_s\varphi)\cdot \mathrm{n},\end{aligned}$$

with

$$H_{\mathcal{M}} = -\nabla_s \cdot \mathrm{n}$$

denoting the mean curvature of $\mathcal{M}$.

In addition, we define

$$c_\Psi = \int_{-1}^{1} \sqrt{2\Psi(s)}\,\mathrm{d}s,$$

which is needed to relate the phase field approach to the sharp interface limit (1), see [11, 52]. Moreover, $\mu : \mathcal{M} \times \mathbb{R}^3 \to \mathbb{R}_{>0}$ is given by γ/β to ensure that (1) is recovered in the sharp interface limit, see [11].

We note that the general model (5) includes several special cases, amongst which are the anisotropic viscous Cahn–Hilliard equation ($\vartheta = 0$), the anisotropic Cahn–Hilliard equation ($\vartheta = \rho = 0$) and the anisotropic Allen–Cahn equation ($a = 0$).

We remark that in applications γ is often chosen spatially homogeneous, so that

$$\gamma(z,p) = \gamma_0(p) \quad \forall z \in \mathcal{M}, p \in \mathbb{R}^3. \tag{6}$$

Using the approach of [19, 20] it can be shown that for the sharp interface limit, $\varepsilon \to 0$, in the sense of Γ-limits it holds that

$$\frac{1}{c_\Psi}\mathcal{E}_\varepsilon \to \mathcal{E}_0,$$

where for a subset E of $\mathcal{M}$ with finite perimeter one defines

$$\mathcal{E}_0(\chi_E) = \int_{\partial E} \gamma(\cdot, \nu_{\partial E}) \,\mathrm{d}\mathcal{H}^1,$$

where $\nu_{\partial E}$ is the outward geodesic normal to $E \subset \mathcal{M}$. In a similar way, the sharp interface limit of the evolution equations (5) can also be investigated. In the planar case this sharp interface limit has been studied in [23, 24, 46, 19, 41, 2], and using ideas from [35, 37] it is possible to translate these ideas to surfaces.

2.3. Weak formulation. The natural weak formulation of (5), with the associated boundary conditions

$$A_p(\cdot, \nabla_s\varphi)\cdot \mathrm{m} = 0 \quad \text{on } \partial\mathcal{M}, \qquad \nabla_s w \cdot \mathrm{m} = 0 \quad \text{on } \partial_N\mathcal{M}, \qquad w = w_D \quad \text{on } \partial_D\mathcal{M},$$

where $\partial\mathcal{M} = \overline{\partial_N\mathcal{M}} \cup \overline{\partial_D\mathcal{M}}$ with relatively open subsets $\partial_N\mathcal{M}$ and $\partial_D\mathcal{M}$ of $\partial\mathcal{M}$ such that $\partial_N\mathcal{M} \cap \partial_D\mathcal{M} = \emptyset$, and where $w_D \in \mathbb{R}$ is a fixed constant, is then given as follows. For $t \in (0,T)$ find $(\varphi, w) \in H^1(\mathcal{M}) \times H^1(\mathcal{M})$ with $w = w_D$ on $\partial_D\mathcal{M}$ such that

$$\vartheta \int_{\mathcal{M}} w_t \chi \,\mathrm{d}\mathcal{H}^2 + \tfrac{1}{2}\lambda \int_{\mathcal{M}} \varphi_t \chi \,\mathrm{d}\mathcal{H}^2 + \int_{\mathcal{M}} \mathcal{K}\nabla_s w \cdot \nabla_s \eta \,\mathrm{d}\mathcal{H}^2 = 0 \qquad \forall\ \chi \in H^1_0(\mathcal{M}), \tag{7a}$$

$$\begin{aligned}\tfrac{1}{2}c_\Psi a \int_{\mathcal{M}} w\eta \,\mathrm{d}\mathcal{H}^2 &= \rho\varepsilon \int_{\mathcal{M}} \mu(\cdot, \nabla_s\varphi)\varphi_t\eta \,\mathrm{d}\mathcal{H}^2 + \alpha\varepsilon \int_{\mathcal{M}} A_p(\cdot, \nabla_s\varphi)\cdot\nabla_s\eta \,\mathrm{d}\mathcal{H}^2 \\ &\quad + \alpha\varepsilon^{-1}\int_{\mathcal{M}} \Psi'(\varphi)\eta \,\mathrm{d}\mathcal{H}^2 \qquad \forall\ \eta \in H^1(\mathcal{M}).\end{aligned} \tag{7b}$$

Above, we used the function space

$$H^1_0(\mathcal{M}) = \{\chi \in H^1(\mathcal{M}) : \chi = 0 \ \text{ on } \partial_D\mathcal{M}\}.$$

3. Properties of anisotropic energies

3.1. Minimal energy directions on the sphere. If one wants to split the unit sphere $\mathbb{S}^2$ into two parts with the same area with a minimal isotropic interfacial energy, then each great circle solves this variational problem. In case that the energy is anisotropic a great circle can lower its interfacial energy by rotating the great circle on $\mathbb{S}^2$. The following lemma discusses the problem of minimizing anisotropic interfacial energy for the problem of splitting the sphere $\mathbb{S}^2$ into two parts with the same area.

LEMMA. 3.1. *Let $\mathcal{M} = \mathbb{S}^2$ and let $\gamma(z,\cdot) = \gamma_0(\cdot)$ for all $z \in \mathcal{M}$. Then the isoperimetric problem*

$$\min\left\{\int_{\partial E} \gamma_0(\nu_{\partial E}) \,\mathrm{d}\mathcal{H}^1 : E \subset \mathcal{M}, \mathcal{H}^2(E) = \tfrac{1}{2}\mathcal{H}^2(\mathcal{M})\right\} \tag{8}$$

is solved by a half sphere E whose boundary ∂E is a great circle with constant outward geodesic normal $\nu_{\partial E} \in \arg\min_{\nu\in\mathcal{M}} \gamma_0(\nu)$.

Proof. As γ_0 is continuous and $\mathcal{M}$ is compact, we deduce that γ_0 attains its minimum on $\mathcal{M}$. Let $\nu_{\min} \in \arg\min_{\nu\in\mathcal{M}} \gamma_0(\nu)$, and let $H \subset \mathbb{R}^3$ be the hyperplane orthogonal to $\nu_{\min}$, with $H_{\leq 0}$ denoting the half space such that $\nu_{\min}$ is its outer normal on $H = \partial H_{\leq 0}$. Then the half sphere $E_{\min} = \mathcal{M} \cap H_{\leq 0}$ solves (8). To see this, we first note that it is an admissible candidate due to $\mathcal{H}^2(\mathcal{M}) = 4\pi$ for the unit sphere. In addition, it holds for any admissible candidate E in (8) that $\mathcal{H}^1(\partial E) \geq \mathcal{H}^1(\partial E_{\min}) = 2\pi$ and hence

$$\int_{\partial E} \gamma_0(\nu_{\partial E})\, \mathrm{d}\mathcal{H}^1 \geq \mathcal{H}^1(\partial E)\gamma_0(\nu_{\min}) \geq \mathcal{H}^1(\partial E_{\min})\gamma_0(\nu_{\min}) = 2\pi\gamma_0(\nu_{\min}),$$

with equality for $E = E_{\min}$, since $\nu_{\partial E_{\min}} = \nu_{\min}$ everywhere on $\partial E_{\min}$. □

3.2. Consistent 2d anisotropies on the unit sphere. In this section we discuss the idea of extending an anisotropy, which is initially defined on just one tangent space of a surface, in a consistent way to all the tangent spaces of the surface. We remark that we only need to define the anisotropy on the tangent spaces and not for all $z \in \mathbb{R}^3$. Assume that at one reference point on the surface an anisotropy density function is given and in certain directions the anisotropy takes a minimal value. Then we want to move the anisotropy along geodesics to other tangent spaces.

This is done in such a way that unit tangent vectors to the geodesic have the same anisotropic density. In fact, this idea can be used for general surfaces. However, we discuss the idea for the unit sphere with the north pole as the reference point, since in this case explicit expressions can be more easily stated. If, for example, on the north pole, we have a six-fold anisotropy, this will remain the case on all the other tangent spaces as well. The procedure will lead to a spatially dependent anisotropy. We point out that for spatially homogeneous anisotropies of the form (6), the strength and shape of the anisotropy may vastly differ between tangent spaces based at different points. Hence the property that the anisotropy remains of the same structure (for example six-fold) will in general not hold true for these anisotropies. We will visualize this phenomenon with some numerical evidence later on.

Due to the hairy ball theorem it is not possible to move an anisotropic energy density in a continuous way along the unit sphere. In fact, we cannot choose tangents at all points on the surface for which the energy density is minimal in such a way that the tangent depends continuously on the point of the surface. We thus have to consider a subset of the sphere. Without loss of generality, assume that $\mathcal{M} \subset \mathbb{S}^2$ with $\partial\mathcal{M} \neq \emptyset$ and such that $e_3 \in \mathcal{M}$ but $-e_3 \notin \mathcal{M}$, so the open manifold is a part of the unit sphere that contains the north pole but not the south pole.

Then for any $z \in \mathcal{M}$ we will construct a rotation matrix $Q(z)$ that rotates the plane spanned by e_3 and z around the axis $e_3 \times z$ by the angle between e_3 and z, so that $Q(z)z = e_3$. The same transformation then also rotates the tangent space $\mathrm{T}_z\mathcal{M}$, and we can evaluate the anisotropy in $Q(z)\mathrm{T}_z\mathcal{M} = \mathrm{T}_{e_3}\mathcal{M} = \mathbb{R}^2 \times \{0\}$. Then we consider

$$\gamma(z, p) = \gamma_0(Q(z)p). \tag{9}$$

Here we have defined an anisotropic density $\gamma_0 : \mathbb{R}^2 \times \{0\} \to \mathbb{R}$, via $\gamma_0(p_1, p_2, p_3) = \widehat{\gamma}(p_1, p_2)$ for an $\widehat{\gamma} : \mathbb{R}^2 \to \mathbb{R}$ that is one-homogeneous.

It is easy to check that the following matrix has the desired properties for $Q(z)$:

$$Q(z) = \begin{pmatrix} z_3 + \frac{z_2^2}{1+z_3} & -\frac{z_1 z_2}{1+z_3} & -z_1 \\ -\frac{z_1 z_2}{1+z_3} & z_3 + \frac{z_1^2}{1+z_3} & -z_2 \\ z_1 & z_2 & z_3 \end{pmatrix} \qquad z \in \mathbb{S}^2 \setminus \{-e_3\}. \tag{10}$$

In particular, it is easy to check that

$$Q(z)Q(z)^T = \mathrm{Id}, \quad Q(z)z = e_3, \quad Q(z)(e_3 \otimes z) = e_3 \otimes z.$$

3.3. BGN-type anisotropies. For the numerical analysis, we restrict ourselves to the following anisotropies of BGN-type

$$\gamma(z,p) = \sum_{\ell=1}^{L} \gamma_\ell(z,p) = \sum_{\ell=1}^{L} [p \cdot G_\ell(z) p]^{\frac{1}{2}}, \qquad \forall\, p \in \mathbb{R}^3, z \in \mathcal{M}, \tag{11}$$

where $G_\ell : \mathcal{M} \to \mathbb{R}^{3\times 3}$, for $\ell = 1, \dots, L$, are functions that map to symmetric and positive definite matrices. For the case that G_ℓ are constant matrices, these anisotropies have first been introduced by Barrett, Garcke and Nürnberg in [4, 5].

LEMMA. 3.2. *Let γ be of the form (11). Then $\gamma(z,\cdot)$ is convex for every $z \in \mathcal{M}$ and the anisotropic operator A satisfies*

(12a)

$$A_p(z,p) \cdot (p-q) \geq \gamma(z,p)[\gamma(z,p) - \gamma(z,q)] \qquad \forall\, p \in \mathbb{R}^3 \setminus \{0\}, q \in \mathbb{R}^3,$$

$$A(z,p) \leq \tfrac{1}{2}\gamma(z,q) \sum_{\ell=1}^{L} [\gamma_\ell(z,q)]^{-1} [\gamma_\ell(z,p)]^2 \qquad \forall\, p \in \mathbb{R}^3, q \in \mathbb{R}^3 \setminus \{0\} \tag{12b}$$

for every $z \in \mathcal{M}$.

Proof. The result follows pointwise from [10, Lemma 2.1]. □

Following [10, 12], we let for every $z \in \mathcal{M}$

$$B(z,q) := \begin{cases} \gamma(z,q) \displaystyle\sum_{\ell=1}^{L} [\gamma_\ell(z,q)]^{-1} G_\ell(z) & q \neq 0, \\ L \displaystyle\sum_{\ell=1}^{L} G_\ell(z) & q = 0. \end{cases}$$

As $A(z,p) = \frac{1}{2}\gamma^2(z,p)$, it clearly holds that

$$B(z,p)p = A_p(z,p) \qquad \forall\, p \in \mathbb{R}^3 \setminus \{0\},$$

and it turns out that approximating $A_p(z,p)$ with $B(z,q)p$ maintains the monotonicity property (12a).

LEMMA. 3.3. *Let γ be of the form (11). Then it holds that*

$$[B(z,q)p] \cdot (p-q) \geq \gamma(z,p)\,[\gamma(z,p) - \gamma(z,q)] \qquad \forall\, p, q \in \mathbb{R}^3, \tag{13}$$

for every $z \in \mathcal{M}$.

Proof. The result follows pointwise from [10, Lemma 2.2]. □

We observe that on letting

$$\widehat{\gamma}(p) = \sum_{\ell=1}^{L} [p \cdot \widehat{G}_\ell p]^{\frac{1}{2}}, \qquad \forall\, p \in \mathbb{R}^2, \tag{14}$$

the anisotropy (9) with (10) falls into the category (11) with the special choices

$$G_\ell(z) = Q^T(z) \begin{pmatrix} \widehat{G}_\ell & 0 \\ 0 & 1 \end{pmatrix} Q(z).$$

4. Finite element approximation

Let $\mathcal{M}^h$ be a polyhedral hypersurface approximating $\mathcal{M}$, and let $\{\mathcal{T}^h\}_{h>0}$ be a family of open triangles with $\mathcal{M}^h = \cup_{\sigma\in\mathcal{T}^h}\overline{\sigma}$. We refer to [16] for more details on polyhedral approximations of surfaces and finite element spaces on polyhedral surfaces. Associated with $\mathcal{T}^h$ is the finite element space

$$S^h = \{\chi \in C(\mathcal{M}^h) : \chi\,|_\sigma \text{ is affine } \forall\, \sigma \in \mathcal{T}^h\}.$$

Let J be the set of nodes of $\mathcal{T}^h$ and $\{p_j\}_{j\in J}$ the coordinates of these nodes. Let $\{\chi_j\}_{j\in J}$ be the standard basis functions for S^h; that is $\chi_j \in S^h$ and $\chi_j(p_i) = \delta_{ij}$ for all $i, j \in J$. A discrete semi-inner product for functions that are piecewise continuous on $\mathcal{T}^h$ can be defined by

$$\langle \eta_1, \eta_2\rangle^h_{\mathcal{M}^h} = \sum_{\sigma\in\mathcal{T}^h} \langle \eta_1, \eta_2\rangle^h_\sigma = \sum_{\sigma\in\mathcal{T}^h} \tfrac{1}{3}|\sigma| \sum_{k=0}^{2} (\eta_1\eta_2)((p_{j_k})^-), \tag{15}$$

with $\{p_{j_k}\}_{k=0}^2$ denoting the vertices of σ, and where we define $\eta((p_{j_k})^-) = \lim_{\sigma\ni q\to p_{j_k}} \eta(q)$, $k = 0, \ldots, 2$. We note that (15) induces the discrete semi-norm $|\eta|_h := [\langle \eta, \eta\rangle^h_{\mathcal{M}^h}]^{\frac{1}{2}}$ on $L^\infty(\mathcal{M}^h)$, that becomes a norm on S^h.

We introduce also

$$K^h = \{\chi \in S^h : |\chi| \le 1\},$$
$$S^h_0 = \{\chi \in S^h : \chi = 0 \text{ on } \partial_D\mathcal{M}^h\} \quad \text{and} \quad S^h_D = \{\chi \in S^h : \chi = w_D \text{ on } \partial_D\mathcal{M}^h\},$$

where $\partial_D\mathcal{M}^h \subset \partial\mathcal{M}^h$ is a suitable approximation of $\partial_D\mathcal{M}$.

In addition to $\mathcal{T}^h$, let $0 = t_0 < t_1 < \ldots < t_{N-1} < t_N = T$ be a partitioning of $[0, T]$ into possibly variable time steps $\tau_n := t_n - t_{n-1}$, $n = 1, \ldots, N$.

4.1. The obstacle potential. Let $\Phi^0 \in K^h$ be an approximation of $\varphi(0)$. Similarly, if $\vartheta > 0$ let $W^0 \in S^h_D$ be an approximation of $w(0)$. Then, for $n \ge 1$, find $(\Phi^n, W^n) \in K^h \times S^h_D$ such that

$$\begin{aligned} &\vartheta \left\langle \frac{W^n - W^{n-1}}{\tau_n}, \chi \right\rangle^h_{\mathcal{M}^h} + \tfrac{1}{2}\lambda \left\langle \frac{\Phi^n - \Phi^{n-1}}{\tau_n}, \chi \right\rangle^h_{\mathcal{M}^h} \\ &\qquad + \langle \mathcal{K}\nabla_s W^n, \nabla_s \chi\rangle^h_{\mathcal{M}^h} = 0 \qquad \forall\, \chi \in S^h_0, \end{aligned} \tag{16a}$$

$$\begin{aligned} &\varepsilon\frac{\rho}{\alpha} \left\langle \mu(\cdot, \nabla_s\Phi^{n-1}) \frac{\Phi^n - \Phi^{n-1}}{\tau_n}, \chi - \Phi^n \right\rangle^h_{\mathcal{M}^h} \\ &\qquad + \varepsilon \left\langle B(\cdot, \nabla_s\Phi^{n-1})\nabla_s\Phi^n, \nabla_s[\chi - \Phi^n] \right\rangle^h_{\mathcal{M}^h} \\ &\qquad \ge \left\langle \tfrac{1}{2} c_\Psi \frac{a}{\alpha} W^n + \varepsilon^{-1}\Phi^{n-1}, \chi - \Phi^n \right\rangle^h_{\mathcal{M}^h} \qquad \forall\, \chi \in K^h. \end{aligned} \tag{16b}$$

REMARK. 4.1. *It is possible to generalize the considered model in the following ways. All of the results presented in this paper remain valid for these generalizations, on using the techniques developed by the authors in* [12].

- *It is possible to consider a phase-dependent* $\mathcal{K}$*, e.g., by defining* $b(s) = \frac{1}{2}(1+s)\mathcal{K}_+ + \frac{1}{2}(1-s)\mathcal{K}_-$*, and replacing* $\mathcal{K}$ *in* (7a) *by* $b(\varphi)$*.*
- *It is possible to consider functions* ϱ *that accelerate the convergence of the phase field model to the sharp interface limit. To this end, the two factors* $\frac{1}{2}$ *in* (7) *are replaced by the coefficients* $\varrho(\varphi)$ *in the two associated integrals, where, e.g.,*

$$\text{(17)} \qquad \textit{(i)}\ \varrho(s) = \tfrac{1}{2}\,, \qquad \textit{(ii)}\ \varrho(s) = \tfrac{1}{2}\,(1-s)\,, \qquad \textit{(iii)}\ \varrho(s) = \tfrac{15}{16}\,(s^2-1)^2\,.$$

- *It is possible to extend the numerical analysis to a more general family of anisotropies. In particular, in place of* (11) *the family of densities*

$$\gamma(z,p) = \left(\sum_{\ell=1}^{L} |\gamma_\ell(z,p)|^r\right)^{\frac{1}{r}}\,, \qquad r \in [1,\infty),$$

can be considered, so that (11) *collapses to the case* $r=1$*. In the case* $r>1$*, the term* $B(\cdot,\nabla_s\Phi^{n-1})$ *in, e.g.,* (16b) *needs to be changed to* $B_r(\cdot,\nabla_s\Phi^{n-1}, \nabla_s\Phi^n)$*, where the matrices* B_r *are defined analogously to the flat and spatially homogeneous case in* [12].

Let

$$\mathcal{E}^h(W,\Phi) = \frac{\vartheta}{2}\,|W-w_D|_h^2 + \frac{\lambda\alpha}{a}\frac{1}{c_\Psi}\left[\tfrac{1}{2}\varepsilon|\gamma(\cdot,\nabla_s\Phi)|_h^2 + \varepsilon^{-1}\langle\Psi(\Phi),1\rangle_{\mathcal{M}^h}^h\right]\,,$$

and define

$$\mathcal{F}^h(W,\Phi) = \mathcal{E}^h(W,\Phi) - \lambda w_D\langle\tfrac{1}{2},1+\Phi\rangle_{\mathcal{M}^h}^h$$

for all $W,\Phi\in S^h$.

THEOREM. 4.2. *Let* γ *be of the form* (11)*. Then there exists a solution* $(\Phi^n,W^n)\in K^h\times S_D^h$ *to* (16)*, where* Φ^n *is unique and* W^n *is unique up to an additive constant. If* $\vartheta>0$ *or* $\partial_D\mathcal{M}^h\neq\emptyset$ *then* W^n *is unique. If* $\vartheta=0$ *and* $\partial_D\mathcal{M}^h=\emptyset$*, then* W^n *is unique if there exists a* $j\in J$ *such that* $|\Phi^n(p_j)|<1$*. In addition, it holds that any solution* $(\Phi^n,W^n)\in K^h\times S_D^h$ *to* (16) *satisfies the stability bound*

$$\begin{aligned}\mathcal{F}^h(W^n,\Phi^n)+\tau_n\langle\mathcal{K}\nabla_s W^n,\nabla_s W^n\rangle_{\mathcal{M}^h}^h + \tau_n\,\frac{\lambda\,\rho}{a}\,\frac{\varepsilon}{c_\Psi}\left|[\mu(\cdot,\nabla_s\Phi^{n-1})]^{\frac{1}{2}}\,\frac{\Phi^n-\Phi^{n-1}}{\tau_n}\right|_h^2 \\ \leq \mathcal{F}^h(W^{n-1},\Phi^{n-1})\,. \qquad \text{(18)}\end{aligned}$$

Proof. The existence and uniqueness results follow analogously to Lemma 3.1 in [12], and so we omit their proof here.

Choosing $\chi = W^n - w_D$ in (16a) and $\chi=\Phi^{n-1}$ in (16b) yields that

$$\begin{aligned}&\vartheta\langle W^n-W^{n-1},W^n-w_D\rangle_{\mathcal{M}^h}^h + \tfrac{1}{2}\lambda\langle\Phi^n-\Phi^{n-1},W^n-w_D\rangle_{\mathcal{M}^h}^h \\ &\qquad + \tau_n\langle\mathcal{K}\nabla_s W^n,\nabla_s W^n\rangle_{\mathcal{M}^h}^h = 0\,, \qquad \text{(19a)}\\ &\varepsilon\frac{\rho}{\alpha}\tau_n^{-1}\langle\mu(\cdot,\nabla_s\Phi^{n-1})[\Phi^n-\Phi^{n-1}],\Phi^{n-1}-\Phi^n\rangle_{\mathcal{M}^h}^h \\ &\qquad + \varepsilon\langle B(\cdot,\nabla_s\Phi^{n-1})\nabla_s\Phi^n,\nabla_s[\Phi^{n-1}-\Phi^n]\rangle_{\mathcal{M}^h}^h \\ &\qquad\qquad \geq \langle\tfrac{1}{2}c_\Psi\frac{a}{\alpha}W^n + \varepsilon^{-1}\Phi^{n-1},\Phi^{n-1}-\Phi^n\rangle_{\mathcal{M}^h}^h. \qquad \text{(19b)}\end{aligned}$$

It follows from (19), on noting the elementary identity

$$2y(y-z) = y^2 - z^2 + (y-z)^2 \qquad \forall\, y, z \in \mathbb{R},$$

and on recalling (13), that

$$\begin{aligned}
&\tfrac{1}{2}\varepsilon|\gamma(\cdot,\nabla_s\Phi^n)|_0^2 - \tfrac{1}{2}\varepsilon^{-1}|\Phi^n|_h^2 + \frac{\vartheta}{2}\frac{a}{\lambda\, a}c_\Psi|W^n - w_D|_h^2 \\
&\quad + \tau_n\varepsilon\frac{\rho}{\alpha}\left|[\mu(\cdot,\nabla_s\Phi^{n-1})]^{\frac{1}{2}}\frac{\Phi^n-\Phi^{n-1}}{\tau_n}\right|_h^2 - w_D\frac{a}{\alpha}c_\Psi\,\langle\tfrac{1}{2},\Phi^n-\Phi^{n-1}\rangle_{\mathcal{M}^h}^h \\
&\quad + \tau_n\frac{a}{\lambda\,\alpha}c_\Psi\langle\mathcal{K}\nabla_s W^n,\nabla_s W^n\rangle_{\mathcal{M}^h}^h \\
&\quad \leq \tfrac{1}{2}\varepsilon|\gamma(\cdot,\nabla_s\Phi^{n-1})|_0^2 - \tfrac{1}{2}\varepsilon^{-1}|\Phi^{n-1}|_h^2 + \frac{\vartheta}{2}\frac{a}{\lambda\, a}c_\Psi|W^{n-1} - w_D|_h^2\,.
\end{aligned}$$

This yields the desired result (18) on adding the constant $\frac{1}{2}\,\varepsilon^{-1}\int_{\mathcal{M}^h} 1\,\mathrm{d}\mathcal{H}^2$ on both sides, and then multiplying the inequality with $\frac{\lambda\,\alpha}{a c_\Psi}$. □

4.2. Smooth potentials. The unconditionally stable approximation (16) for the obstacle potential (4) can be easily adapted to the case of a smooth potential such as (3). Such approximations rely on a convex/concave splitting of $\phi = \Psi'$, i.e., $\phi = \phi^+ + \phi^-$ with

$$\pm(\phi^\pm)'(s) \geq 0 \quad \forall\, s \in \mathbb{R}\,.$$

For the quartic potential (3) the natural choices are

$$\phi^+(s) = s^3 \quad \text{and} \quad \phi^-(s) = -s\,, \tag{20}$$

and for simplicity we restrict our attention to that case. Details on how to deal with more general potentials can be found in [12].

As before, given $\Phi^0 \in K^h$ and, if $\vartheta > 0$, $W^0 \in S_D^h$, for $n \geq 1$, find $(\Phi^n, W^n) \in S^h \times S_D^h$ such that

$$\begin{aligned}
&\vartheta\left\langle\frac{W^n - W^{n-1}}{\tau_n},\chi\right\rangle_{\mathcal{M}^h}^h + \tfrac{1}{2}\lambda\left\langle\frac{\Phi^n-\Phi^{n-1}}{\tau_n},\chi\right\rangle_{\mathcal{M}^h}^h \\
&\qquad + \langle\mathcal{K}\nabla_s W^n,\nabla_s\chi\rangle_{\mathcal{M}^h}^h = 0 \quad \forall\,\chi\in S_0^h, \qquad \text{(21a)}\\
&\varepsilon\frac{\rho}{\alpha}\left\langle\mu(\cdot,\nabla_s\Phi^{n-1})\frac{\Phi^n-\Phi^{n-1}}{\tau_n},\chi\right\rangle_{\mathcal{M}^h}^h + \varepsilon\left\langle B(\cdot,\nabla_s\Phi^{n-1})\nabla_s\Phi^n,\nabla_s\chi\right\rangle_{\mathcal{M}^h}^h \\
&\qquad + \varepsilon^{-1}\left\langle\phi^+(\Phi^n),\chi\right\rangle_{\mathcal{M}^h}^h \\
&\qquad = \left\langle\tfrac{1}{2}c_\Psi\frac{a}{\alpha}W^n - \varepsilon^{-1}\phi^-(\Phi^{n-1}),\chi\right\rangle_{\mathcal{M}^h}^h \qquad \forall\,\chi\in S^h. \qquad \text{(21b)}
\end{aligned}$$

THEOREM. 4.3. *Let γ be of the form* (11). *Let Ψ be given by* (3) *and let* (20) *hold. Then there exists a unique solution $(\Phi^n, W^n) \in S^h \times S_D^h$ to* (21). *Moreover, the solution satisfies the stability bound* (18).

Proof. The existence and uniqueness results follow analogously to Theorem 3.8 in [12]. The proof of the stability bound (18) is similar to the proof of Theorem 4.2, making use of the convex/concave splitting $\Psi' = \phi = \phi^+ + \phi^-$. □

5. Numerical results

We implemented the scheme (16) with the help of the finite element toolbox ALBERTA, see [55]. To increase computational efficiency, we employ adaptive meshes, which have a finer mesh size $h_f \approx \frac{1}{N_f}$ within the diffuse interfacial regions

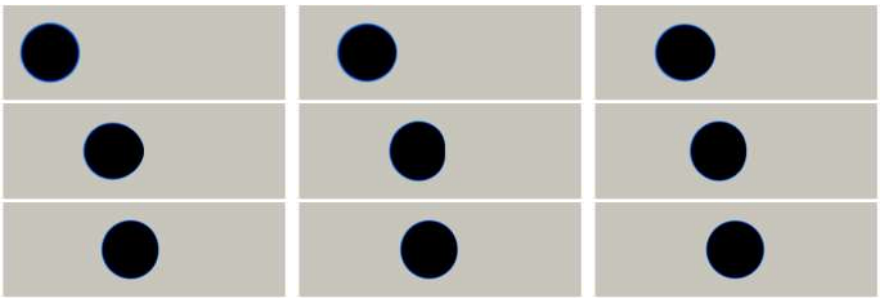

FIGURE 2. ($\varepsilon = (16\pi)^{-1}$) Solutions for the Cahn–Hilliard equation in the case of a spatially inhomogeneous energy in the plane. Snapshots of the evolutions at times $t = 0,\ 0.1,\ 0.2,\ 0.3,\ 0.4,\ 0.5,\ 0.6,\ 0.7,\ 2$.

and a coarser mesh size $h_c \approx \frac{1}{N_c}$ away from them, with $N_f, N_c \in \mathbb{N}$, see [18, 17] for a more detailed description in the planar case. For the solution of the nonlinear systems of equations we employ the iterative solvers discussed in [12].

Unless otherwise stated, for the physical parameters in (5) we choose $\vartheta = \rho = 0$, $\lambda = \mathcal{K} = a = \alpha = 1$, $\mu = 1$ and (4) for the potential Ψ. In addition, we employ uniform time steps $\tau_n = \tau$, $n = 1, \dots, N$.

5.1. Spatially inhomogeneous anisotropies in 2d. In this section we consider the special case $\mathcal{M} \subset \mathbb{R}^2 \times \{0\} \subset \mathbb{R}^3$, i.e., we reformulate evolutions in $\mathbb{R}^2$ within the framework of this paper.

Then, on $\mathcal{M} = (-\frac{3}{2}, \frac{3}{2}) \times (-\frac{1}{2}, \frac{1}{2}) \times \{0\}$ we use the spatially weighted isotropic surface energy

$$\gamma(z, p) = (0.01 + |z|)|p|.$$

As the initial interface we choose a circle of radius 0.3 centred at $(-1, 0)^T$. Clearly, the interface can reduce its energy by moving towards a circle centred at the origin, which we conjecture to be the global minimizer for this setting. The evolution for the solutions from our scheme (16) can be seen in Figure 2. Here we let $\varepsilon = (16\pi)^{-1}$, $N_c = 32$, $N_f = 512$ and $\tau = 10^{-4}$.

5.2. Spatially homogeneous anisotropies in 3d. In this section we consider anisotropies of the form (6).

5.2.1. Simulations for Lemma 3.1. We choose as anisotropy the density (22)

$$\gamma(\cdot, p) = \gamma_0(p) = l_\delta(R_2(\tfrac{\pi}{2})\, p) + w \sum_{\ell=1}^{3} l_\delta(R_1(\tfrac{\ell\pi}{3})\, p),\ \delta = 0.01,\ \begin{cases} w = \frac{1}{\sqrt{3}} & \text{(a)} \\ w = 1 & \text{(b)} \\ w = \frac{1}{2\sqrt{3}} & \text{(c)} \end{cases},$$

where $R_1(\theta) = \begin{pmatrix} \cos\theta & \sin\theta & 0 \\ -\sin\theta & \cos\theta & 0 \\ 0 & 0 & 1 \end{pmatrix}$, $R_2(\theta) = \begin{pmatrix} \cos\theta & 0 & \sin\theta \\ 0 & 1 & 0 \\ -\sin\theta & 0 & \cos\theta \end{pmatrix}$ and $l_\delta(p) = \big[\delta^2 |p|^2 + p_1^2 (1 - \delta^2)\big]^{\frac{1}{2}}$. The Wulff shapes for (22) are shown in Figure 3. We recall from [36] that for a given anisotropy γ_0 the boundary of its Wulff shape is the solution of the isoperimetric problem for $\mathcal{E}_0(\Gamma) = \int_\Gamma \gamma_0(\nu)\, \mathrm{d}\mathcal{H}^2$. Hence they are often used to visualize the properties of γ_0. We note that for $\delta = 0$, the densities (22) represent crystalline anisotropies, whose Wulff shapes are given by hexagonal prisms, cf. [9,

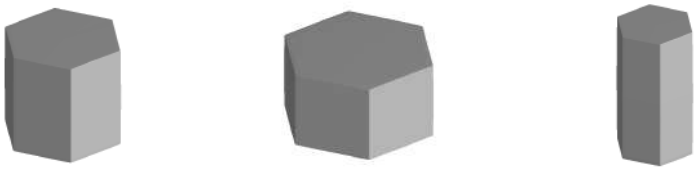

FIGURE 3. The Wulff shapes for (22)(a), (22)(b) and (22)(c).

Fig. 3]. The coefficients in (22)(a) are chosen such that, in the limit $\delta = 0$, the eight admissible normal directions all have the same energy, while in (22)(b) and (22)(c) the two normals $\pm e_3$ have a smaller/larger energy than the other six directions.

We use the anisotropy (22)(b) with $\delta = 10^{-2}$ to numerically investigate the statement from Lemma 3.1. To this end, we choose as initial interface a perturbed great circle on the unit sphere, that lies in a hyperplane that makes a certain fixed angle θ with the $x-z$-plane. In particular, in Figure 4 we show simulations for $\theta = 10^\circ, 30^\circ, 60^\circ$. Here we let $\varepsilon = (16\pi)^{-1}$, $N_c = 1$, $N_f = 128$ and $\tau = 10^{-4}$. We note that each simulation settles on a great circle on the sphere. Here we note that as $\nu_{\min} = e_3$, the equator has the lowest energy of all the great circles, and so if the initial curve on $\mathcal{M}$ is sufficiently inclined, that global minimizer is indeed reached by the evolution. For only small deviations from a north-south great circle, the evolutions settle on that local minimizer instead. We remark that the discrete steady state solutions exhibit final discrete energies $\mathcal{F}^h(W^n, \Phi^n)$ of 12.7, 6.7 and 6.7, respectively. This once again confirms that the equator has the lowest energy.

5.2.2. Convergence experiment on the unit sphere. We use the rotationally symmetric solution for the Mullins–Sekerka problem on the unit sphere from [52] for a convergence experiment for our approximations as $\varepsilon \to 0$, see also [7].

We consider an annulus domain on the unit sphere, which is bounded by two circles on the lower half with radii $1 > R_1(t) > R_2(t) > 0$. This uniquely defines angles $\theta_i(t) \in (\frac{\pi}{2}, \pi)$ such that $R_i(t) = \sin\theta_i(t)$ and $h_i(t) = \cos\theta_i(t) < 0$ denotes the heights of the two circles. That means at any given time, the annulus will enclose a surface area of $2\pi(h_1(t) - h_2(t)) = 2\pi(\cos\theta_1(t) - \cos\theta_2(t))$. Hence $a_0 := \cos\theta_1(0) - \cos\theta_2(0) = \cos\theta_1(t) - \cos\theta_2(t)$ is an invariant, and so

$$\theta_2(t) = \arccos(\cos\theta_1(t) - a_0), \tag{23}$$

which means that the ODE system for (θ_1, θ_2) from [52] can be reduced to a scalar differential equation. The former is given by

$$\lambda\theta_i'(t) = -\frac{c_+(t)}{\sin\theta_i(t)}, \ i = 1, 2, \tag{24a}$$

where

$$c_+(t) = -\alpha\frac{\cot\theta_1(t) + \cot\theta_2(t)}{\ln(\tan\frac{\theta_1(t)}{2}) - \ln(\tan\frac{\theta_2(t)}{2})}. \tag{24b}$$

Combining (24) with (23) yields a scalar differential equation for θ_1.

For the initial data we choose $R_1(0) = 2R_2(0) = 0.8$, so that $h_1(0) = -0.6$ and $h_2(0) = -\sqrt{0.84}$, respectively. In order to get the same time scale as in [52], we use $\alpha = \frac{\sqrt{2}}{3}$ and $\lambda = 2$ for these experiments, and we visualize the phase field energies

$$\tfrac{1}{2}\varepsilon|\nabla_s\Phi^m|_h^2 + \varepsilon^{-1}\langle\Psi(\Phi^m), 1\rangle_{\mathcal{M}^h}^h,$$

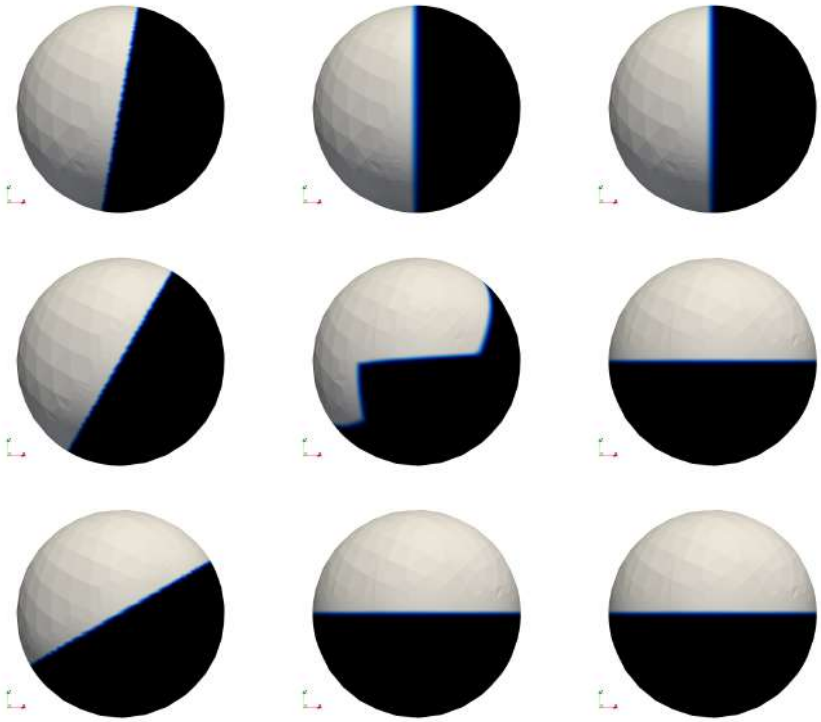

FIGURE 4. ($\varepsilon = (16\pi)^{-1}$) Anisotropic Cahn–Hilliard equation on a sphere. Snapshots of the evolutions at times $t = 0, 1, 5$ (from left to right). The initial data approximates a great circle within a hyperplane that is tilted by $10°, 30°, 60°$ (from top to bottom).

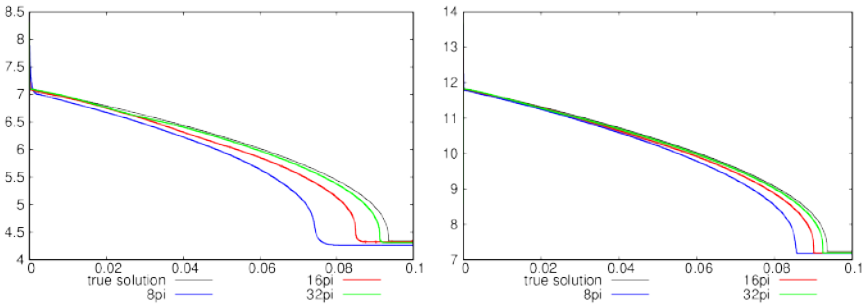

FIGURE 5. ($\alpha = \frac{\sqrt{2}}{3}$, $\lambda = 2$) Energy plots for (21) (left) and (16) (right) for $\varepsilon = (8\pi)^{-1}$, $\varepsilon = (16\pi)^{-1}$ and $\varepsilon = (32\pi)^{-1}$, compared to the sharp interface solution.

for deceasing values of ε, compared to the energy $2\pi c_\Psi(\sin\theta_1(t_m) + \sin\theta_2(t_m))$ of the sharp interface solution. See Figure 5, where our numerical results confirm the asymptotic convergence as $\varepsilon \to 0$ to the sharp interface limit.

5.2.3. Spinodal decomposition on closed surfaces. In this section we consider $\varepsilon = (16\pi)^{-1}$, as well as $N_c = 1$, $N_f = 128$, $\tau = 10^{-6}$. We use different surface

FIGURE 6. ($\varepsilon = (16\pi)^{-1}$) Spinodal decomposition on a sphere, for $\gamma(p) = |p|$. Snapshots of the evolutions at times $t = 10^{-4}, 2 \times 10^{-4}, 5 \times 10^{-4}, 10^{-3}, 0.01, 1$.

FIGURE 7. ($\varepsilon = (16\pi)^{-1}$) Spinodal decomposition on a sphere, for (22)(a). Snapshots of the evolutions at times $t = 2 \times 10^{-4}, 5 \times 10^{-4}, 10^{-3}, 5 \times 10^{-3}, 0.01, 2$.

FIGURE 8. ($\varepsilon = (16\pi)^{-1}$) Spinodal decomposition on a sphere, for (22)(b). Snapshots of the evolutions at times $t = 2 \times 10^{-4}, 5 \times 10^{-4}, 10^{-3}, 2 \times 10^{-3}, 0.01, 1$.

energy densities for evolutions that start from a random mixture with mean zero and values in $[-0.1, 0.1]$. At first we choose the unit sphere $\mathcal{M} = \mathbb{S}^2$. In this isotropic case, we observe the well known spinodal decomposition patterns, see Figure 6. When we use the anisotropy (22)(a), for which in the limit $\delta = 0$ the normals $\nu = \pm e_3$ have the same energy density as the other six main facet normals of the crystalline Wulff shape, during the spinodal decomposition we can observe corners, see Figure 7. Note that the spatially homogeneous anisotropy leads to hexagonal symmetries only at the two poles, whereas the patterns near the equator resemble squares. The corresponding evolution for the anisotropy (22)(b) is shown in Figure 8. Here it can be seen that $\nu = \pm e_3$ is now the preferred normal direction, and so the interfaces very quickly align with it. As a final experiment, we also use the anisotropic density (22)(c), see Figure 9 for the numerical results. Now the opposite effect can be observed: since the normals $\nu = \pm e_3$ are relatively expensive, they are avoided by the developing interfaces. We also observe that out of the four spinodal decomposition experiments, only two settle on a global energy minimizer as described in Lemma 3.1. We conjecture that the final shape for the other two simulations is made up of "straight" segments that are aligned with the Wulff shape, in the sense that their normal vectors correspond to directions with minimal energy density. The anisotropic nature of the surface energy then seems to make it impossible to go from this local minimizer to one of the global ones.

We end this subsection with a simulation on a surface that is the boundary of a nonconvex domain. In particular, we base $\mathcal{M}^h$ on a rescaled version of the biconcave disk obtained in [13, Fig. 8]. The total dimensions of $\mathcal{M}^h$ are about $0.28 \times 1 \times 1$. On this surface we repeat the simulation from Figure 7. The results of this new numerical experiment are shown in Figure 10, where we once again

FIGURE 9. ($\varepsilon = (16\pi)^{-1}$) Spinodal decomposition on a sphere, for (22)(c). Snapshots of the evolutions at times $t = 2 \times 10^{-4}, 5 \times 10^{-4}, 10^{-3}, 5 \times 10^{-3}, 0.01, 1$.

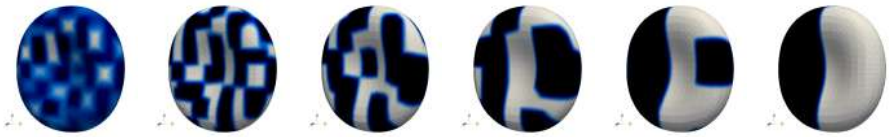

FIGURE 10. ($\varepsilon = (16\pi)^{-1}$) Spinodal decomposition on a biconcave disk, for (22)(a). Snapshots of the evolutions at times $t = 10^{-4}, 2 \times 10^{-4}, 5 \times 10^{-4}, 10^{-3}, 5 \times 10^{-3}, 0.01$.

observe the squared patterns due to the alignment of the surface with respect to the Wulff shape of the anisotropy (22)(a).

5.2.4. Crystal growth on a sphere cap. In this section we use the hexagonal, spatially homogeneous anisotropic density (22)(a) for computations of crystal growth on a sphere cap. Here the sphere cap $\mathcal{M} \subset \mathbb{S}^2$ is given by

$$\mathcal{M} = \left\{ \begin{pmatrix} 0 \\ 0 \\ 1 \end{pmatrix} \right\} \cup \left\{ \begin{pmatrix} \frac{z_1}{|z|} \cos\theta(z) \\ \frac{z_2}{|z|} \cos\theta(z) \\ \sin\theta(z) \end{pmatrix} : z = \begin{pmatrix} z_1 \\ z_2 \\ 0 \end{pmatrix} \in \mathbb{R}^3, 0 < |z| \leq 1 \right\},$$

where $\theta(z) = (\frac{\pi}{2} + \frac{\pi}{18})(1 - |z|) - \frac{\pi}{18}$.

For the physical parameters, similarly to [12, Fig. 9], we choose $\alpha = 0.03$, $\rho = 0.01$ and $w_D = -8$.

Some first computations are shown in Figure 11, where for $\varepsilon = (32\pi)^{-1}$ we select the discretization parameters $N_c = 16$, $N_f = 128$ and $\tau = 10^{-5}$. We start with an initial seed of radius $r_0 = 0.02$: either at the north pole, or on the equator on the x-axis, or on the equator on the y-axis. The evolutions in Figure 11 make it clear that the hexagonal aspect of the anisotropy (22)(a) only comes to the fore at the north pole. At the equator, on the other hand, we see interfaces with a four-fold symmetry, consistent with the Wulff shape displayed in Figure 3. We remark that these computations are for (17)(ii), compare with [12, (2.11)(ii)]. Repeating the same simulations for (17)(i) leads to the creation of boundary layers, which is why we prefer the choice (17)(ii) here and from now. We refer to [12] for a more detailed discussion of this aspect.

Having established that for the homogeneous hexagonal anisotropies in this section it is beneficial for six-fold structures to start with a seed at the north pole, we present a few more computations with a seed of radius $r_0 = 0.02$ at the north pole. Then for different physical parameters, we obtain slightly different evolutions. But note that what they all have in common is that the crystal will initially grow sixth arms, but these will then often display non-hexagonal sidearms and structures. The simulations shown in Figure 12 are for $w_D = -12$, with either $\rho = \alpha = 0.01$, $\rho = 10\alpha = 0.01$ or $\rho = \alpha = 0.001$, respectively. Here we let $\varepsilon = (32\pi)^{-1}$ and $N_c = 32$, $N_f = 256$ and $\tau = 10^{-5}$. For the next simulations we left everything

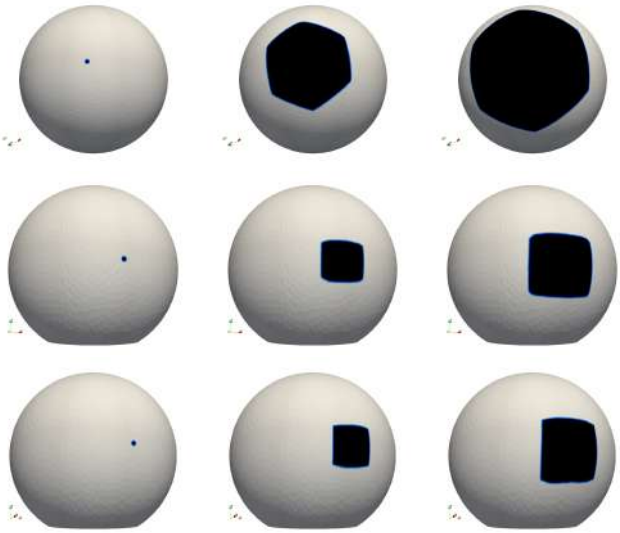

FIGURE 11. ($\varepsilon = (32\pi)^{-1}$) Parameters as in [12, Fig. 9], but here $\varepsilon = (32\pi)^{-1}$ and $w_D = -8$. Starting seed on top (top), at the front (middle) and on the right (bottom). Displayed times are $t = 0, 0.05, 0.1$ (top) and $t = 0, 0.01, 0.02$ (middle and bottom).

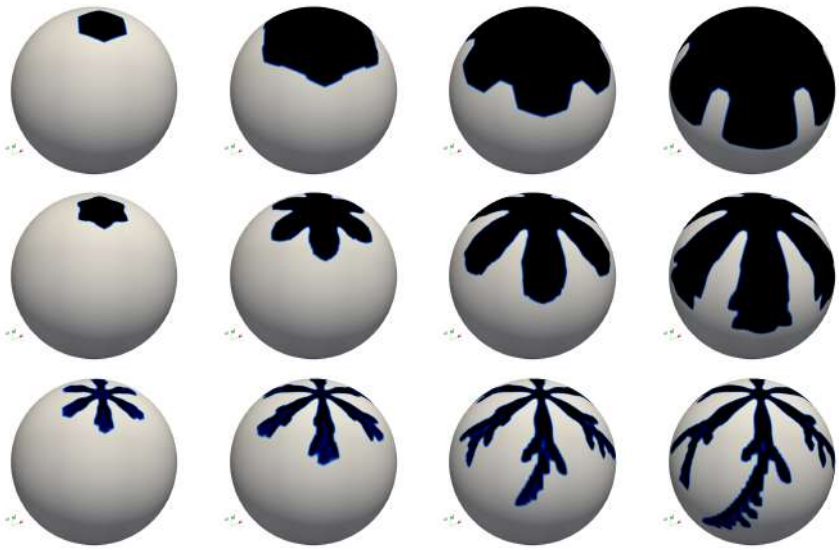

FIGURE 12. ($\varepsilon = (32\pi)^{-1}$) Parameters as in Figure 11 but $w_D = -12$ and: $\rho = \alpha = 0.01$ (top), $\rho = 10\alpha = 0.001$ (middle) and $\rho = \alpha = 0.001$ (bottom). Displayed times are $t = 0.01, 0.05, 0.08, 0.12$ (top), $t = 0.01, 0.03, 0.06, 0.09$ (middle) and $t = 0.01, 0.02, 0.03, 0.04$ (bottom).

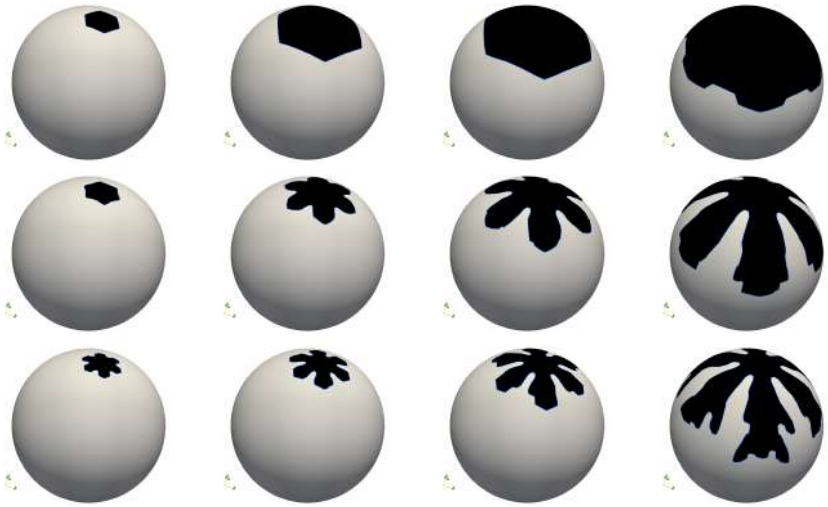

FIGURE 13. ($\varepsilon = (64\pi)^{-1}$) Parameters as in Figure 12 but with $w_D = -8$ and starting from a smaller initial seed, with radius $r_0 = 0.005$. Displayed times are $t = 0.01, 0.05, 0.08, 0.14$ (top), $t = 0.01, 0.03, 0.06, 0.012$ (middle) and $t = 0.01, 0.02, 0.04, 0.1$ (bottom).

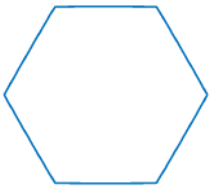

FIGURE 14. The Wulff shape for (25).

unchanged, apart from $w_D = -8$ and starting from a smaller seed, with radius $r_0 = 0.005$. As a consequence we also change the values of $\varepsilon = (64\pi)^{-1}$, $N_c = 32$, $N_f = 512$ and $\tau = 2.5 \times 10^{-6}$. The new results are shown in Figure 13. We stress once more that if the seed would not be placed at the north pole, or if the ambient anisotropy would be rotated so that the tangent space at the north pole is not aligned with the six-fold symmetry, then the resulting growth would not show the desired six-fold symmetric patterns.

5.3. Consistent 2d anisotropies on the unit sphere. In this subsection we present some numerical evidence in support of the construction of consistent anisotropies along a surface as proposed in §3.2. We first repeat the simulations in Figure 11, but now for the anisotropy (9) with (14), for $L = 3$, the usual 2d hexagonal anisotropy from, e.g., [4, 7, 10, 12], i.e.,

$$\widehat{\gamma}(p) = \sum_{\ell=1}^{3} l_\delta(\widehat{R}_1(\tfrac{\ell\pi}{3})\, p), \tag{25}$$

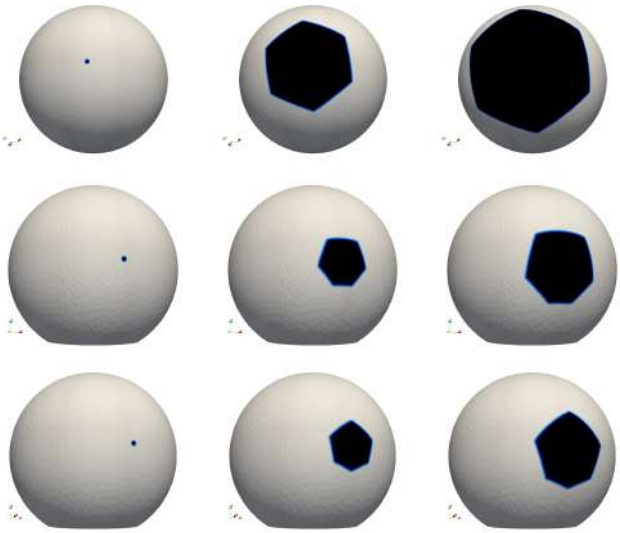

FIGURE 15. ($\varepsilon = (32\pi)^{-1}$) Parameters as in Figure 11, but for the anisotropy (9) with (25). Starting seed on top (top), at the front (middle) and on the right (bottom). Displayed times are $t = 0, 0.05, 0.1, 0.4$ (top) and $t = 0, 0.01, 0.02, 0.05$ (middle and bottom).

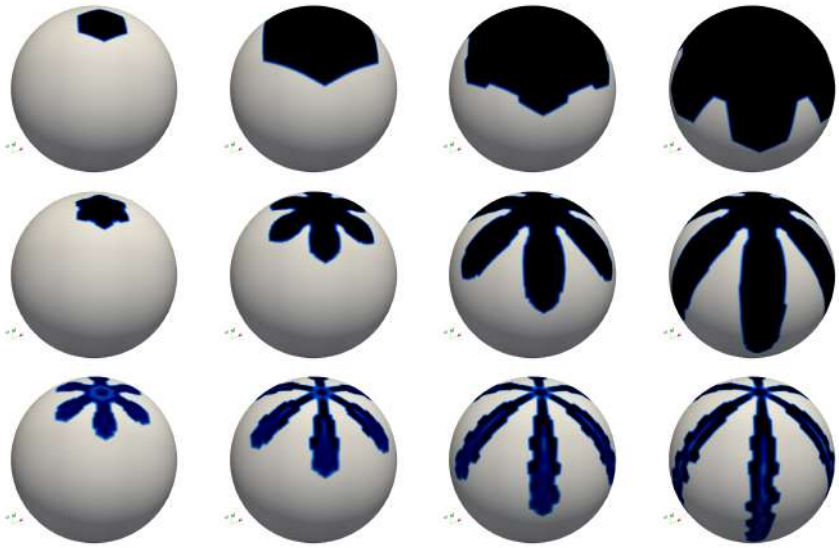

FIGURE 16. ($\varepsilon = (32\pi)^{-1}$) Parameters as in Figure 12, but with the anisotropy (9) with (25).

with $\widehat{R}_1(\theta) := \begin{pmatrix} \cos\theta & \sin\theta \\ -\sin\theta & \cos\theta \end{pmatrix}$, similarly to (22). We visualize the Wulff shape of (25) in Figure 14.

The numerical results are shown in Figure 15, and the difference to Figure 11 is obvious. While the two simulations for the initial seed at the north pole are

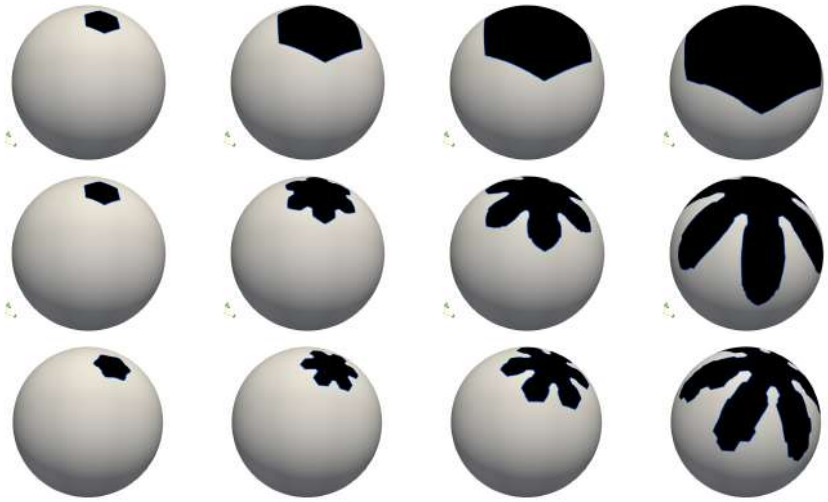

FIGURE 17. ($\varepsilon = (64\pi)^{-1}$) Parameters as in Figure 13, but with the anisotropy (9) with (25).

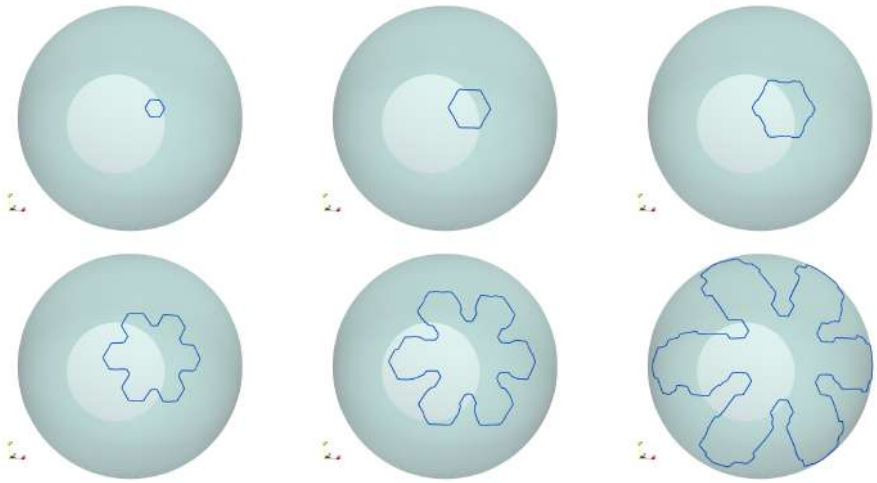

FIGURE 18. ($\varepsilon = (64\pi)^{-1}$) The results from the final row in Figure 17 displayed from a different point of view, and at times $t = 0.001, 0.005, 0.01, 0.02, 0.04, 0.1$.

qualitatively very close, the seeds that start on the equator have very different evolutions. In Figure 11, the seeds grow into a quadrilateral interface, while in Figure 15 these also grow hexagonally. The explanation can be found in the Wulff shape of (22), which for tangent spaces on the equator of the sphere will lead to four-fold structures, rather than six-fold structures at the two poles.

With this arguably more realistic anisotropy for ice crystal growth on a sphere in place, we can repeat the simulations in Figure 12 now for this new anisotropy. The results are shown in Figure 16, where for the last row we observe the development

FIGURE 19. An experiment with three initial seeds. Each crystal grows symmetrically to the others.

of some mushy regions, suggesting that ε was not chosen sufficiently small to resolve the physics of the underlying sharp interface problem.

When we repeat the simulations in Figure 13 for the new anisotropy these mushy regions disappear, see Figure 17. Observe that compared to the dendritic growth in the former case, the new simulations show the natural six-fold growth also way beyond the equator. In fact, the interface growths in Figure 18 look very similar to the 2d simulations in [7, 8, 9].

In Figure 19 we show a snapshot of a simulation that started from three initial seeds. Due to the symmetric arrangement of the seeds, the three crystals continue to grow symmetrically.

Overall the simulations in this subsections underline the ability of the anisotropies introduced in §3.2 to model a hexagonal crystal growth on all parts of the unit sphere segment, in contrast the the results for the simpler global anisotropies seen in, e.g., §5.2.4.

References

[1] S. F. Ahmadi, S. Nath, C. M. Kingett, P. Yue and J. B. Boreyko, How soap bubbles freeze, Nat. Commun., 10 (2019) 2531.

[2] M. Alfaro, H. Garcke, D. Hilhorst, H. Matano and R. Schätzle, Motion by anisotropic mean curvature as sharp interface limit of an inhomogeneous and anisotropic Allen–Cahn equation, Proc. Roy. Soc. Edinburgh Sect. A, 140 (2010) 673–706.

[3] E. Bänsch, K. Deckelnick, H. Garcke and P. Pozzi, Interfaces: Modeling, Analysis, Numerics, volume 51 of *Oberwolfach Seminars*, Birkhäuser/Springer, Cham (2023).

[4] J. W. Barrett, H. Garcke and R. Nürnberg, Numerical approximation of anisotropic geometric evolution equations in the plane, IMA J. Numer. Anal., 28 (2008) 292–330.

[5] J. W. Barrett, H. Garcke and R. Nürnberg, A variational formulation of anisotropic geometric evolution equations in higher dimensions, Numer. Math., 109 (2008) 1–44.

[6] J. W. Barrett, H. Garcke and R. Nürnberg, Numerical approximation of gradient flows for closed curves in $\mathbb{R}^d$, IMA J. Numer. Anal., 30 (2010) 4–60.

[7] J. W. Barrett, H. Garcke and R. Nürnberg, On stable parametric finite element methods for the Stefan problem and the Mullins–Sekerka problem with applications to dendritic growth, J. Comput. Phys., 229 (2010) 6270–6299.

[8] J. W. Barrett, H. Garcke and R. Nürnberg, Numerical computations of faceted pattern formation in snow crystal growth, Phys. Rev. E, 86 (2012) 011604.

[9] J. W. Barrett, H. Garcke and R. Nürnberg, Finite-element approximation of one-sided Stefan problems with anisotropic, approximately crystalline, Gibbs–Thomson law, Adv. Differential Equations, 18 (2013) 383–432.

[10] J. W. Barrett, H. Garcke and R. Nürnberg, On the stable discretization of strongly anisotropic phase field models with applications to crystal growth, ZAMM Z. Angew. Math. Mech., 93 (2013) 719–732.
[11] J. W. Barrett, H. Garcke and R. Nürnberg, Phase field models versus parametric front tracking methods: Are they accurate and computationally efficient?, Commun. Comput. Phys., 15 (2014) 506–555.
[12] J. W. Barrett, H. Garcke and R. Nürnberg, Stable phase field approximations of anisotropic solidification, IMA J. Numer. Anal., 34 (2014) 1289–1327.
[13] J. W. Barrett, H. Garcke and R. Nürnberg, A stable numerical method for the dynamics of fluidic membranes, Numer. Math., 134 (2016) 783–822.
[14] J. W. Barrett, H. Garcke and R. Nürnberg, Finite element approximation for the dynamics of fluidic two-phase biomembranes, ESAIM Math. Model. Numer. Anal., 51 (2017) 2319–2366.
[15] J. W. Barrett, H. Garcke and R. Nürnberg, Numerical approximation of curve evolutions in Riemannian manifolds, IMA J. Numer. Anal., 40 (2020) 1601–1651.
[16] J. W. Barrett, H. Garcke and R. Nürnberg, Parametric finite element approximations of curvature driven interface evolutions, in A. Bonito and R. H. Nochetto, editors, Handb. Numer. Anal., volume 21, Elsevier, Amsterdam (2020) pages 275–423.
[17] J. W. Barrett, R. Nürnberg and V. Styles, Finite element approximation of a phase field model for void electromigration, SIAM J. Numer. Anal., 42 (2004) 738–772.
[18] L. Baňas and R. Nürnberg, Finite element approximation of a three dimensional phase field model for void electromigration, J. Sci. Comp., 37 (2008) 202–232.
[19] G. Bellettini and M. Paolini, Anisotropic motion by mean curvature in the context of Finsler geometry, Hokkaido Math. J., 25 (1996) 537–566.
[20] G. Bellettini, M. Paolini and S. Venturini, Some results on surface measures in calculus of variations, Ann. Mat. Pura Appl. (4), 170 (1996) 329–357.
[21] J. F. Blowey and C. M. Elliott, The Cahn–Hilliard gradient theory for phase separation with non-smooth free energy. Part I: Mathematical analysis, European J. Appl. Math., 2 (1991) 233–280.
[22] D. Caetano and C. M. Elliott, Cahn–Hilliard equations on an evolving surface, European J. Appl. Math., 32 (2021) 937–1000.
[23] G. Caginalp, An analysis of a phase field model of a free boundary, Arch. Rational Mech. Anal., 92 (1986) 205–245.
[24] G. Caginalp and X. Chen, Convergence of the phase field model to its sharp interface limits, European J. Appl. Math., 9 (1998) 417–445.
[25] J. W. Cahn and J. E. Taylor, Surface motion by surface diffusion, Acta Metall. Mater., 42 (1994) 1045–1063.
[26] K. Deckelnick, G. Dziuk and C. M. Elliott, Computation of geometric partial differential equations and mean curvature flow, Acta Numer., 14 (2005) 139–232.
[27] K. Deckelnick and R. Nürnberg, A novel finite element approximation of anisotropic curve shortening flow, Interfaces Free Bound., 25 (2023) 671–708.
[28] K. Deckelnick and R. Nürnberg, An unconditionally stable finite element scheme for anisotropic curve shortening flow, Arch. Math. (Brno), 59 (2023) 263–274.
[29] Q. Du and X. Feng, The phase field method for geometric moving interfaces and their numerical approximations, in A. Bonito and R. H. Nochetto, editors, Handb. Numer. Anal., volume 21, Elsevier, Amsterdam (2020) pages 425–508.
[30] Q. Du, L. Ju and L. Tian, Finite element approximation of the Cahn–Hilliard equation on surfaces, Comput. Methods Appl. Mech. Engrg., 200 (2011) 2458–2470.
[31] G. Dziuk and C. M. Elliott, Surface finite elements for parabolic equations, J. Comput. Math., 25 (2007) 385–407.
[32] C. M. Elliott, Approximation of curvature dependent interface motion, in I. S. Duff and G. A. Watson, editors, The state of the art in numerical analysis (York, 1996), volume 63 of *Inst. Math. Appl. Conf. Ser. New Ser.*, Oxford Univ. Press, New York (1997) pages 407–440.
[33] C. M. Elliott and R. Schätzle, The limit of the anisotropic double-obstacle Allen–Cahn equation, Proc. Roy. Soc. Edinburgh Sect. A, 126 (1996) 1217–1234.
[34] C. M. Elliott and R. Schätzle, The limit of the fully anisotropic double-obstacle Allen–Cahn equation in the nonsmooth case, SIAM J. Math. Anal., 28 (1997) 274–303.
[35] C. M. Elliott and B. Stinner, A surface phase field model for two-phase biological membranes, SIAM J. Appl. Math., 70 (2010) 2904–2928.
[36] I. Fonseca and S. Müller, A uniqueness proof for the Wulff theorem, Proc. Roy. Soc. Edinburgh Sect. A, 119 (1991) 125–136.

[37] H. Garcke, J. Kampmann, A. Rätz and M. Röger, A coupled surface-Cahn–Hilliard bulk-diffusion system modeling lipid raft formation in cell membranes, Math. Models Methods Appl. Sci., 26 (2016) 1149–1189.
[38] H. Garcke, P. Knopf, R. Nürnberg and Q. Zhao, A diffuse-interface approach for solid-state dewetting with anisotropic surface energies, J. Nonlinear Sci., 33 (2023) 34.
[39] H. Garcke, P. Knopf and J. Wittmann, The anisotropic Cahn–Hilliard equation: Regularity theory and strict separation properties, Discrete Contin. Dyn. Syst. Ser. S, 16 (2023), 3622–3660.
[40] H. Garcke, B. Nestler and B. Stinner, A diffuse interface model for alloys with multiple components and phases, SIAM J. Appl. Math., 64 (2004) 775–799.
[41] H. Garcke, B. Stoth and B. Nestler, Anisotropy in multi-phase systems: a phase field approach, Interfaces Free Bound., 1 (1999) 175–198.
[42] P. Gera and D. Salac, Cahn–Hilliard on surfaces: A numerical study, Appl. Math. Lett., 73 (2017) 56–61.
[43] C. Gräser, R. Kornhuber and U. Sack, Time discretizations of anisotropic Allen–Cahn equations, IMA J. Numer. Anal., 33 (2013) 1226–1244.
[44] R. Kobayashi, Modeling and numerical simulations of dendritic crystal growth, Phys. D, 63 (1993) 410–423.
[45] C. Lee, S. Yoon, J. Park, H. Kim, Y. Li, D. Jeong, S. Kim, S. Kwak and J. Kim, Phase-field computations of anisotropic ice crystal growth on a spherical surface, Comput. Math. Appl., 125 (2022) 25–33.
[46] G. B. McFadden, A. A. Wheeler, R. J. Braun, S. R. Coriell and R. F. Sekerka, Phase-field models for anisotropic interfaces, Phys. Rev. E (3), 48 (1993) 2016–2024.
[47] K. Mikula and D. Ševčovič, Computational and qualitative aspects of evolution of curves driven by curvature and external force, Comput. Vis. Sci., 6 (2004) 211–225.
[48] K. Mikula and D. Ševčovič, Evolution of curves on a surface driven by the geodesic curvature and external force, Appl. Anal., 85 (2006) 345–362.
[49] M. Olshanskii, Y. Palzhanov and A. Quaini, A scalar auxiliary variable unfitted FEM for the surface Cahn–Hilliard equation, J. Sci. Comput., 97 (2023), 57.
[50] L. Ortellado and L. R. Gómez, Phase field modeling of dendritic growth on spherical surfaces, Frontiers in Materials, 7 (2020) 163.
[51] P. Pozzi, Anisotropic curve shortening flow in higher codimension, Math. Methods Appl. Sci., 30 (2007) 1243–1281.
[52] A. Rätz, A benchmark for the surface Cahn–Hilliard equation, Appl. Math. Lett., 56 (2016) 65–71.
[53] A. Rätz and A. Voigt, PDE's on surfaces—a diffuse interface approach, Commun. Math. Sci., 4 (2006) 575–590.
[54] A. Saxena and T. Lookman, Kinetics of phase separation on curved manifolds: soft matter, Phys. D, 133 (1999) 416–426.
[55] A. Schmidt and K. G. Siebert, Design of Adaptive Finite Element Software: The Finite Element Toolbox ALBERTA, volume 42 of *Lecture Notes in Computational Science and Engineering*, Springer-Verlag, Berlin (2005).
[56] J.-K. Seong, W.-K. Jeong and E. Cohen, Anisotropic geodesic distance computation for parametric surfaces, in 2008 IEEE International Conference on Shape Modeling and Applications, pages 179–186.
[57] J.-K. Seong, W.-K. Jeong and E. Cohen, Curvature-based anisotropic geodesic distance computation for parametric and implicit surfaces, Vis. Comput., 25 (2009) 743–755.
[58] I. Steinbach, Phase-field models in materials science, Modelling Simul. Mater. Sci. Eng., 17 (2009) 073001.
[59] I. Steinbach and H. Salama, Lectures on Phase Field, Springer Nature, Cham, Switzerland (2023).
[60] S. Thomas, R. Cassoni and C. MacArthur, Aircraft anti-icing and de-icing techniques and modeling, J. Aircr., 33 (1996) 841–854.
[61] S. Torabi, J. Lowengrub, A. Voigt and S. Wise, A new phase-field model for strongly anisotropic systems, Proc. R. Soc. Lond. Ser. A Math. Phys. Eng. Sci., 465 (2009) 1337–1359.
[62] A. A. Wheeler and G. B. McFadden, A ξ-vector formulation of anisotropic phase-field models: 3D asymptotics, European J. Appl. Math., 7 (1996) 367–381.
[63] S. Yoon, J. Park, J. Wang, C. Lee and J. Kim, Numerical simulation of dendritic pattern formation in an isotropic crystal growth model on curved surfaces, Symmetry, 12 (2020) 1155.

[64] Y. Zhuang, M. Zou, N. Carr and T. Ju, Anisotropic geodesics for live-wire mesh segmentation, Computer Graphics Forum, 33 (2014) 111–120.

Fakultät für Mathematik, Universität Regensburg, 93040 Regensburg, Germany
E-mail: harald.garcke@ur.de

Dipartimento di Mathematica, Università di Trento, 38123 Trento, Italy
E-mail: robert.nurnberg@unitn.it